JPL D-104254 L1B
ATBD-EMIT-01

Earth Mineral dust source InvesTigation (EMIT)

EMIT L1B Algorithm: Calibrated Radiance at Sensor

Theoretical Basis

David R. Thompson and Robert O. Green, and others
Jet Propulsion Laboratory, California Institute of Technology

Version 1.0

April 2020

Jet Propulsion Laboratory
California Institute of Technology
Pasadena, California 91109-8099

Change Log

Version	Date	Comments
0.1	July 27, 2019	Initial Draft
0.2	Sept. 29, 2019	Candidate version for peer review
0.3	Dec. 16, 2019	Changes in response to peer review
0.4	Jan 26, 2020	Added output products
1.0	April 10, 2020	Pre-CDR Science Peer Review

TABLE OF CONTENTS

1. Key Teammembers

A large number of individuals contributed to the development of the algorithms, methods, and implementation of the L1b approach for EMIT. The primary contributors are the following:

- David R. Thompson (Jet Propulsion Laboratory) – EMIT Co-I, Instrument Scientist
- Robert O. Green (Jet Propulsion Laboratory) – Mission PI, Radiometric modeling
- Michael Eastwood (Jet Propulsion Laboratory) – Calibration and Detector Technology
- Christine Bradley (Jet Propulsion Laboratory) – Optical design and Models
- Sarah Lundeen (Jet Propulsion Laboratory) – Science Data System Lead
- Randy Pollock (Jet Propulsion Laboratory – Instrument Systems Engineer

2. Historical Context and Background on the EMIT Mission and its Instrumentation

Mineral dust radiative forcing is the single largest uncertainty in aerosol direct radiative forcing (USGCRP and IPCC). Mineral dust is a principal contributor to direct radiative forcing over arid regions, impacting agriculture, precipitation, and desert encroachment around the globe. However, we have poor understanding of this effect due to uncertainties in the dust composition. Dust radiative forcing is highly dependent on its mineral-specific absorption properties, and the current range of iron oxide abundance in dust source models (0 – 7 wt%) translates into a 460% uncertainty in regional radiative forcing predicted by Earth System Models (ESMs). Meanwhile, soil samples from North Africa regions - important sources of mineral dust - contain up to 30 wt% iron oxide. The National Aeronautics and Space Administration (NASA) recently selected the Earth Mineral Dust

Source Investigation (EMIT) to close this knowledge gap. EMIT will launch an instrument to the International Space Station (ISS) to directly measure and map the mineral composition of critical dust-forming regions worldwide.

The EMIT Mission will use imaging spectroscopy across the visible shortwave (VSWIR) range to reveal distinctive mineral signatures, enabling rigorous mineral detection, quantification, and mapping. The overall investigation aims to achieve two objectives.

1. Constrain the sign and magnitude of dust-related RF at regional and global scales. EMIT achieves this objective by acquiring, validating and delivering updates of surface mineralogy used to initialize ESMs.
2. Predict the increase or decrease of available dust sources under future climate scenarios. EMIT achieves this objective by initializing ESM forecast models with the mineralogy of soils exposed within at-risk lands bordering arid dust source regions.

The EMIT instrument is a Dyson imaging spectrometer that will resolve the distinct absorption features of iron oxides, clays, sulfates, carbonates, and other dust-forming minerals with contiguous spectroscopic measurements in the visible to short wavelength infrared region of the spectrum. EMIT will map mineralogy with a spatial sampling to detect minerals at the one hectare scale and coarser, ensuring accurate characterization the mineralogy at the grid scale required by ESMs. EMIT's fine spatial sampling will resolves the soil exposed within hectare-scale agricultural plots and open lands of bordering arid regions, critical to understanding feedbacks caused by mineral dust arising from future changes in land use, land cover, precipitation, and regional climate forcing.

Data Product	Description	Initial Availability	Median Latency Post-delivery	NASA DAAC
Level 0	Raw collected telemetry	4 months after IOC	2 months	LP DAAC
Level 1a	Reconstructed, depacketized, uncompressed data, time referenced, annotated with ancillary information reassembled into scenes.	4 months after IOC	2 months	LP DAAC
Level 1b	Level 1a data processed to sensor units including geolocation and observation geometry information	4 months after IOC	2 months	LP DAAC
Level 2a	Surface reflectance derived by screening clouds and correction for atmospheric effects.	8 months after IOC	2 months	LP DAAC
Level 2b	Mineralogy derived from fitting reflectance spectra, screening for non-mineralogical components.	8 months after IOC	2 months	LP DAAC
Level 3	Gridded map of mineral composition aggregated from level 2b with uncertainties and quality flags	11 months after IOC	2 months	LP DAAC
Level 4	Earth System Model runs to address science objectives	16 months after IOC	2 months	LP DAAC

Table 1: EMIT Data Product Hierarchy

The EMIT Project is part of the Earth Venture-Instrument (EV-I) Program directed by the Program Director of the NASA Earth Science Division (ESD). EMIT is comprised of a Visible/Shortwave Infrared Dyson imaging spectrometer adapted for installation on the International Space Station (ISS). It will be installed on Flight Releasable Attachment Mechanism (FRAM) of an ExPRESS

Logistics Carrier (ELC) on the ISS, in a site formally designated ELC 1 FRAM 8. NASA has assigned management of the Project to the Jet Propulsion Laboratory of the California Institute of Technology. The EMIT Payload is scheduled to be installed on the ELC 1 FRAM 8 in 2021.

Table 1 above describes the different data products to which the EMIT Mission will provide to data archives. This document describes the "Level 1B" radiometric and spectral calculations.

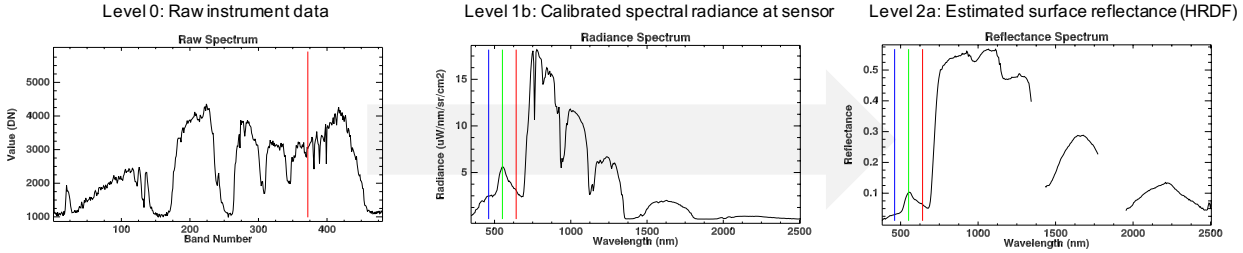

Figure 1: Representative spectra from the EMIT analysis, data product levels 0, 1B, and 2A.

This document describes the theoretical basis for the algorithm producing EMIT's calibrated "Level 1b" product, which reports spectral radiance measured at the sensor (Figure 1). It begins from reconstructed "Level 1a" products consisting of raw detector counts already recorded, downlinked, and reassembled from instrument telemetry. It then applies spectral and radiometric calibration to produce uniform radiance cubes for subsequent geolocalization. These will next be analyzed with inversion using physically-motivated surface/atmosphere models to estimate surface reflectance, the "Level 2A" product, for later analysis by mineral detection and mapping algorithms. These stages are all instantiated in the EMIT science product generation software operating at the Jet Propulsion Laboratory, California Institute of Technology. Finally, we incorporate mineral maps into Earth System modeling to evaluate Radiative Forcing (RF) impacts. Figure 2 shows a diagram of the entire workflow.

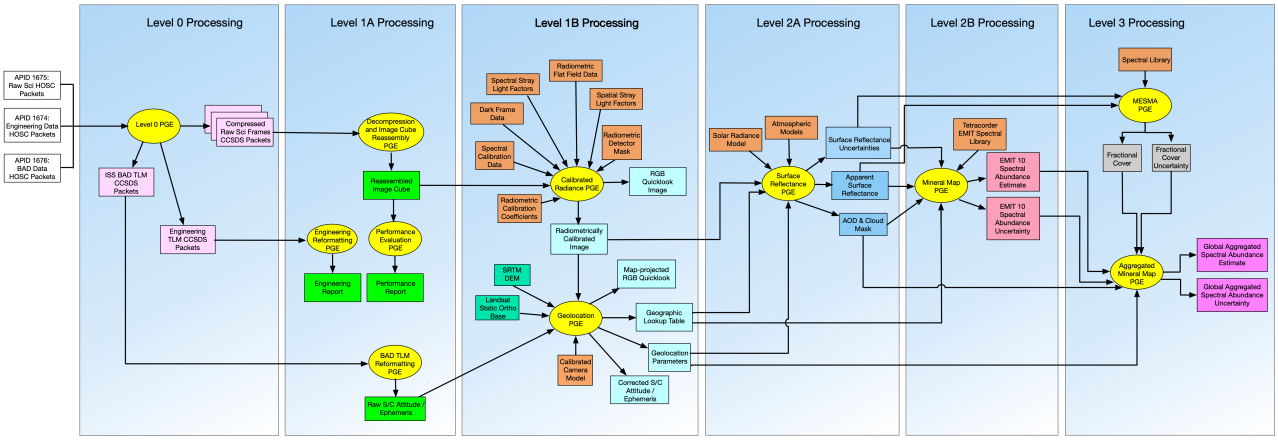

Figure 2. High-level workflow of the EMIT science data system.

3 Algorithm rationale and prior validation

The EMIT Level 1B approach comes from a long history of analyses on airborne precursor instruments such as NASA's "Classic" Airborne Visible Infrared Imaging Spectrometer (AVIRIS-C, Green et al., 1998) and its next generation counterpart (AVIRIS-NG, Thompson et al., 2017). Such analyses have been conducted in dozens of campaigns over decades of successful operations. Very similar methods have been used in prior space missions to planetary objects including NASA's M^3 Lunar exploration (Green et al., 2011) and the CRISM mission to Mars (Murchie et al., 2004).

The EMIT Instrument calibration, including its noise model and various aspects of the analysis chain, does demand some specific changes due to the unique nature of the instrument. EMIT consists of a Dyson-type spectrometer with f-number 1.8, providing high optical photon throughput. It is based on a calcium fluoride refractive block, curved grating, slit, and a focal-plane array with 1240 cross track elements and 480 spectral elements. A matched telescope contains two fixed silver mirrors for magnification. Figure 3 illustrates the optical layout by tracing ray bundles at 1440 nm. EMIT measures incident illumination at the sensor, the radiance ($\mu m\ nm^{-1}\ cm^{-2}\ sr^{-1}$), the "Level 1B" products from which analysts can then infer the reflectance using a model of photon transport in the atmosphere. Atmospheric correction methods vary, but the technology is sufficiently mature to provide good results over benign haze-free conditions and observing geometries (Thompson et al., 2015, 2018a, 2018b). However, high-accuracy surface reflectance estimates rest on a foundation of high-fidelity, calibrated radiance spectra (Thompson et al., 2019).

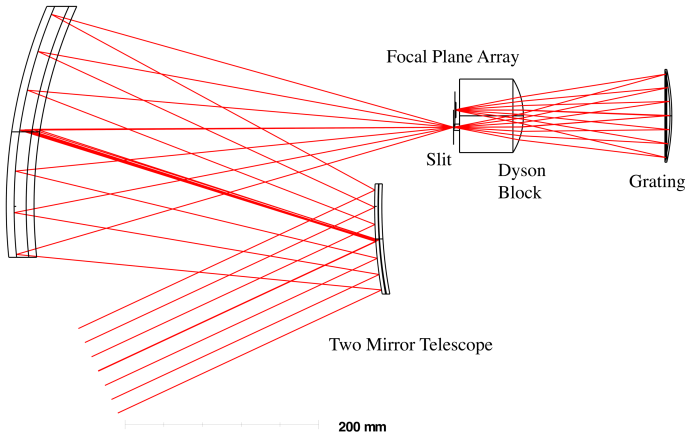

Figure 3: EMIT optical design

The system's spectral and radiometric response properties are fully-characterized in advance using laboratory measurements to provide a default calibration applicable as soon as EMIT begins operations on the ISS. Later in-flight calibration and validation (Thompson et al., 2018a, 2018b) is possible as needed, and will follow standard practice established historically by instruments such as Hyperion; it will be used to validate, and if needed, refine, laboratory calibrations.

We have generally adopted the AVIRIS-NG approach to calibration here (Chapman et al., 2019). It may be possible, as the EMIT mission progresses, to eliminate some unneeded corrections if the instrument proves more stable or sensitive than that earlier sensor. However, we have adopted a conservative approach and are planning to implement all standard corrections for EMIT.

4. Algorithm description

4.1 Input data

While the EMIT input and output data products delivered to the DAAC use their formatting conventions, the system operates internally on data products stored as binary data cubes with detatched human-readable ASCII header files. The precise formatting convention adheres to the ENVI standard, which can be accessed (Dec. 2019) at https://www.harrisgeospatial.com/docs/ENVIHeaderFiles.html. The header files all consist of data fields in equals-sign-separated pairs, and describe the layout of the file. The specific input files needed for the L1b stage are:

1. A **dark frame** cube, derived from the temporally-closest acquisition of a dark target by the EMIT instrument, sized to the focal plane array, Band-Sequential (BSQ), with size 480x1280, in single-precision floating point.
2. A **DN** cube, organized in band-interleaved-by-line format, of digital numbers. The scenes can have arbitrary length but each independent frame (vertical line) of data has size 480 x 1280 and appears as 2 byte unsigned integers. The cube is arranged in Band Interleaved by Line (BIL) format.
3. A **Spectral Calibration file** provided as a 480 x 1280 x 4 binary float 32, BSQ interleave with detached ASCII header. It contains the Center wavelength in first channel, uncertainty in second, FWHM in third, uncertainty in FWHM in fourth channel.
4. **Spectral Stray Light Factors,** a 480 x 480 binary float 32 file, BSQ with detached ASCII header, used in the stray light PSF conditioning as described below as matrix A^+ in equation 9.
5. **Radiometric Calibration Coefficients**, a 480 x 1280 x 100 binary float 32, BSQ interleave with detached ASCII header, listing small relative multiplicative per-channel radiometric corrections that refine the RCC-predicted radiance value. This list should be close to unity. With uncertainties.
6. **Radiometric Flat Field** file, the flat field coefficients as described below, as a 480x 1280 x 2 binary float 32 file, BSQ with detached ASCII header.
7. **Radiometric Detector** Mask, a single 16 bit signed integer frame, with detatched ASCII header, containing information about the location of known bad pixels. Zero indicates good pixels. <1 indicates bad pixels and number of contiguous bad pixels in the spectrum. >1 indicated row and column masked pixels. For more information on how this file is used, we refer the reader to Chapman et al (2019).
8. **Spatial Stray Light Factors** file. This is the spatial analogue to 4, above. It is used similarly to the A^+ matrix in equation 9.

Table 2 Below enumerates all products.

Input Calibration file	Format	Format	Interpretation
Radiometric Dark Signal	480 x 1280 float 32, BSQ interleave with detached ASCII header	Offset value to be subtracted from each element before radiometric analysis.	From unilluminated portion of orbit and masked detector elements.
DN	480 x 1280 x N uint16, BIL interleave with detached ASCII header	Instrument observation data (L1a)	One scene of instrument record data from the L1a product.
Spectral Calibration	480 x 1280 x 4 binary float 32, BSQ interleave with detached ASCII header	Center wavelength in first channel, uncertainty in second, FWHM in third, uncertainty in FWHM in fourth	Spectral calibration and uncertainty (nanometers)
Spectral Stray Light Factors	480 x 480 binary float 32 file, BSQ, detached ASCII header	Correction matrices	Brings response functions towards Gaussian
Radiometric Calibration Coefficients	480 x 1280 x 100 binary float 32, BSQ interleave with detached ASCI header	uW /cm2/ nm / sr piecewise description	Maps DN to radiance with allowance for non linearity
Radiometric Flat Field	480x 1280 x 2 binary float 32 file, BSQ, detached ASCII header	Small relative radiometric corrections that refine the RCC-predicted radiance value. Should be close to unity. With uncertainties.	Fine correction of radiometric coefficient. Nominally from pseudoinvarient targets.
Radiometric Detector Mask	480 x 1280 16 integer file, BSQ, detached ASCII header	Zero indicates good pixels. <1 indicates bad pixels and number of contiguous bad pixels in the spectrum. >1 indicated row and column masked pixels.	From laboratory calibration measurements. Updated as needed.
Spatial Stray Light Factors	1280 x 1280 binary float 32 file, BSQ, detached ASCII header	Correction matrices	Brings response functions towards Gaussian

Table 2: Input files

Further information on the development of these values appears in the calibration section below.

4.2 Theoretical description

Calibrating the raw instrument data involves two basic steps. The first performs absolute radiometric calibration, transforming DNs at the instrument into units of radiance using their calibrated radiometric response, while correcting for any electronic artifacts and bad FPA pixels. The second stage corrects for various instrument optical effects and assigns an absolute spectral wavelength calibration. These steps appear in Figure 4 below, adapted from Chapman et al. (2019).

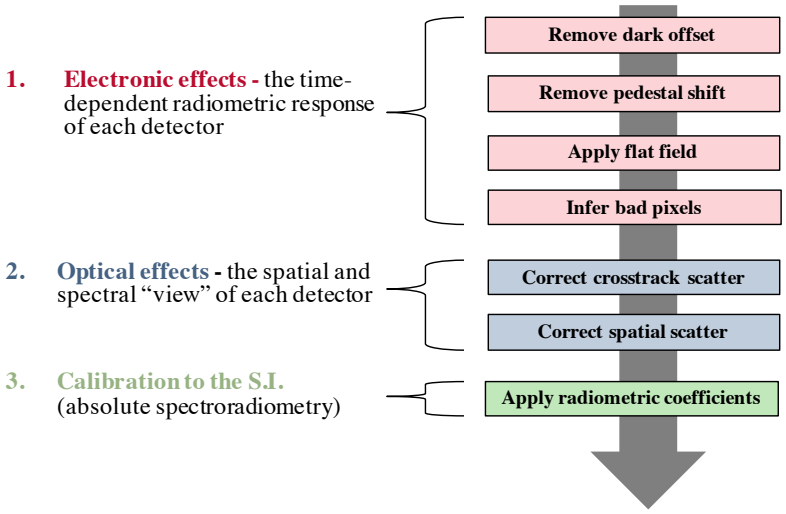

Figure 4: L1b Calibration procedure

The overall goal of electronic and optical corrections is to produce the FPA response that would have been observed by an "ideal" instrument, i.e., one having perfect Gaussian spectral response functions and perfectly linear radiometry. The following sections describe each step in greater detail.

Stage I Calibration – basic radiometry

The conversion from DNs to measured radiance uses the linear relationship:

$$L_{FPA}(\lambda, x) = [D(\lambda, x) - \alpha(\lambda, x)]\beta(\lambda, x) \quad (1)$$

where $L_{FPA}(\lambda,x)$ is a function of wavelength λ and cross-track spatial location x. The terms $\alpha(\lambda,x)$ and $\beta(\lambda,x)$ represent the offset and gain measured in Digital Numbers (DNs), respectively. The offset $\alpha(\lambda,x)$ can be further decomposed into an additive combination:

$$\alpha(\lambda, x) = \alpha_{dark}(\lambda, x) + \alpha_{ped}(x) \quad (2)$$

where $\alpha_{dark}(\lambda,x)$ corresponds to the dark current and $\alpha_{ped}(x)$ corresponds to a distortion known as the pedestal shift. We estimate the dark current parameters using designated dark current frames acquired during each orbit. They represent changes that arise from the thermal environment of the instrument on timescales of minutes or hours, depending on the length of acquisition. The baseline approach for EMIT is to use the temporally closest dark current estimate for each acquisition, but interpolating between multiple estimates may provide superior results if needed. The dark current is then estimated and subtracted from each spectrum independently.

An illumination of any region of the FPA may result in an overall shift in the dark current everywhere, known as the pedestal shift. The pedestal shift is characterized independently for each

frame using the non-illuminated edges of the focal plane, which have been physically masked to ensure no stray light contamination. From this characterization, the pedestal shift is estimated via robust least-squares minimization with following linear function of location across the focal plane array:

$$\alpha_{dark}(\lambda, x) = A\lambda + Bx + C \tag{3}$$

Depending on the characteristics of the Focal Plane Array as observed in flight, it may be preferable to apply a per-spectrum pedestal correction, which is fit independently using masked channels:

$$\alpha_{ped}(x) = A(x)\lambda + C(x) \tag{4}$$

The mission reserves both options, and uses measured performance to select the best results. The gain term $\beta(\lambda,x)$ in Equation 1 is a radiometric calibration coefficient (RCC) and can be further decomposed into the multiplicative form:

$$\beta(\lambda, x) = \beta_{rcc}(\lambda)\beta_{flat}(\lambda, x) \tag{5}$$

where $\beta_{RCC}(\lambda)$ is the spatially independent calibration coefficient and $\beta_{flat}(\lambda,x)$ is the spatially dependent flat field. Here we note that the average flat field value in each spectral channel, that is the average of all cross track positions, is constrained to unity:

$$\left[\frac{1}{|\mathcal{X}|}\sum_{x\in\mathcal{X}}\beta_{flat}(\lambda, x))\right] = 1 \quad \forall\lambda \tag{6}$$

The EMIT focal plane array, like most detectors, contains isolated pixels or clusters of pixels with a response that differs significantly from their neighbors. Some do not respond at all. While the number of these bad pixels is small — less than 0.1% of the total — the single-channel artifacts they create are a significant contaminant since they create outlier spectra that are obvious in data statistics and derived products. identify these bad pixels at commissioning through the traditional method of using a flat field measurement produced with a uniformly illuminated spatially-uniform calibration object, such as an integration sphere. We flag outlier pixels manually by thresholding their standard deviations. In typical HgCdTe detectors like that of EMIT, the resulting bad pixel list remains stable after commissioning.

While bad pixels are only cataloged once, they must be corrected independently in each image frame using a statistically appropriate method of interpolating pixel values for bad elements (Chapman et al., 2019). Simple interpolation in the spectral dimension is inadequate, since it does not respect the channel- wise structure of real spectra; it distorts the underlying data statistics which must remain pristine for downstream analyses. Instead, we exploit the spectral shapes of nearby locations that are similar to the spectrum undergoing correction. Given a spectrum s' with bad pixels, we identify the most similar spectrum in its image frame, s^*, and then fit a linear relationship between the radiance values of s^* and s'. Similarity between spectra is defined by the spectral angle:

$$\mathbf{s}^* = \text{argmin}_s \frac{\langle \mathbf{s}', \mathbf{s}\rangle}{|\mathbf{s}'|_2\ |\mathbf{s}|_2} \tag{7}$$

After identifying s^*, we predict the missing values in the incomplete spectrum by fitting a regression model that maps spectral points of s^* onto the incomplete spectrum s', minimizing least squares error with standard closed-form expression. Naturally, we exclude the bad channels from this calculation. We then apply the map to predict the missing values in s'.

Stage II Calibration – optical correction and wavelength assignment

The measured radiance $L_M(\lambda)$ represents the best estimate of light at the detector using the nominal Gaussian line shape which is measured in the laboratory. However, any physical instrument exhibits some degree of non-Gaussian response behavior. These perturbations often take the form of "thick tails" to the response function; even at levels which are three or four orders of magnitude below the peak, they can reduce the spectral contrast of features such as sharp atmospheric absorptions (Thompson et al. 2018). Such distortions arise because, in practice, each incoming ray is partially scattered through interactions with different areas of the optical system and the scattered light ultimately propagates onto multiple areas of the detector array. These unwanted signals cause spatial and spectral blurring within the scene.

After standard radiometric calibrations, we estimate the stray spectral response function as described in Thompson et al. (2018). We begin by defining a matrix representing the incoming at-aperture radiance for a large number of wavelengths d, where $d \gg 480$, at each of the 1240 cross-track locations, and write it as L_A. The Gaussian nominal spectral response function is represented by a linear operator H of size $480 \times d$. We posit a vertical stack of single spectral response functions per output channel can transform the at-aperture radiance, L_A, into the nominal instrument output becomes:

$$\mathbf{L_n} = \mathbf{H}\mathbf{L_A} \tag{8}$$

Due to the fact that the matrix H has a rank less than d, the nominal spectral response function is not invertible and it eliminates spectral details finer than the instrument's ideal resolution. The resultant nominal response L_N contains dimensions of a data frame, a 480×1240 matrix with 480 spectral channels and 640 cross-track positions.

The measured response $\mathbf{L_M}$ can be modeled by distorting the nominal response L_N by some stray spectral response, modeled for convenience as a 480×480 linear operator G. In addition, a small Gaussian random variable ε is added, which combines the read noise, dark noise, and photon shot noise in quadrature. This allows the following operations:

$$\begin{aligned}
\mathbf{L_M} &= \mathbf{G}\mathbf{H}\mathbf{L_A} + \mathbf{H}\mathbf{L_A} + \epsilon \\
\mathbf{L_M} &= \mathbf{G}\mathbf{L_N} + \mathbf{L_N} + \epsilon \\
\mathbf{L_M} &= [\mathbf{G} + \mathbf{I}]\mathbf{L_N} + \epsilon \\
\mathbf{L_M} &= \mathbf{A}\mathbf{L_N} + \epsilon
\end{aligned} \tag{9}$$

where A corresponds to the stray spectral response operator with an identity matrix added along it's diagonal, as performed in prior work by Zong et al. (2006). We define a correction operator to recover the nominal data frame which would have been found under the nominal spectral response function by inversion of the stray spectral response functions influence. The Moore-Penrose pseudoinverse $\mathbf{A^+ = (A^T A)^{-1} A^T}$ guarantees $\mathbf{A{+}A = I}$. The resulting most probable unperturbed measurement $\hat{\boldsymbol{L}}$ is:

$$\hat{\mathbf{L}} = \mathbf{A}^{+}\mathbf{L_m} \tag{10}$$

We perform this operation independently in both spatial and spectral dimensions. This limits the correction to blurring functions that are separable, i.e. representable as independent operators applied sequentially in the spatial and spectral dimensions. This is not an onerous constraint in practice and we find that families of Gaussian distributions and other isotropic or separable functions are a sufficient palette to represent Point Spread Function (PSF) broadening effects.

Finally, we apply a wavelength assignment. Our initial solution uses monochromatic laser sources of known wavelengths used in laboratory characterization measurements, which then feed a linear wavelength calibration model. If needed we refine the initial wavelength calibration after operation

begins with flight data using a single uniform shift to match atmospheric absorption features in the top of atmosphere (TOA) reflectance spectrum. The basic procedure is described by Thompson et al. (2015a) but we reproduce it here for completeness. The features of the TOA reflectance spectrum ρ are formed from the radiance measurement $\mathbf{L_M}$ at wavelength λ, after normalizing for extra-terrestrial solar irradiance F and solar zenith θ:

$$\rho(\lambda) = \frac{\pi L_M(\lambda)}{F(\lambda)\cos(\theta)} \tag{11}$$

We model the TOA spectrum as a locally-linear continuum attenuated by gaseous absorption of the 760 nm oxygen band and the 820 nm water vapor band. The spectral attenuation is governed by a Beer-Lambert law based on the gas absorption coefficient κ(λ) obtained from a 20 layer model atmosphere:

$$\hat{\rho}(c) = h(\phi_1)[\phi_2 e - \phi_3 \kappa(\phi_4 + \lambda) + \phi_5(\phi_4 + \lambda)] \tag{12}$$

where φ_i is the free parameter optimized by the fitting procedure. The function $h(\varphi_1)$ is the convolution with a Gaussian Spectral Response Function (SRF) with a FWHM given by φ_1. φ_2 is the local continuum level at 100%, and φ_3 represents the absorption path length. φ_4 represents the wave- length shift, the parameter we sought to recover, and the local continuum slope is represented by φ_5. We fit these parameters using a Nelder-Mead simplex algorithm (Nelder & Mead 1965). Figure 5 below shows an example of this procedure for the Airborne Visible Infrared Imaging Spectrometer (AVIRIS-NG) precursor airborne instrument, for which the model matches the measured spectrum with a residual error less than 1%, placing it within the limits of the spectrometer's radiometric accuracy.

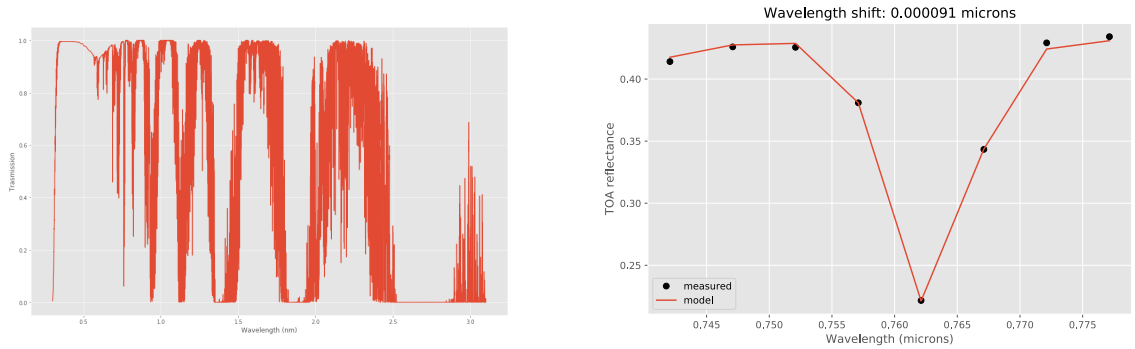

Figure 5: (Left) Typical atmospheric transmission spectrum. (Right) Wavelength tuning result using AVIRIS-NG airborne data over a calibration/validation site.

4.3 Practical considerations

The radiometric code is implemented in C, and operates independently on single frames of data read and written one at a time. The operations are all computationally fast and tractable. The largest single operations are the corrections for stray spectral and spatial response, which involve multiplication of spectra and rows by matrices sized 480x480 and 1280x1280 respectively. Even these are tractable. All other data dependencies are instrument parameters set during commissioning (such as the pedestal shift coefficients in Equation 3 above) are encoded in the software version directly using software best practice for holding data; they are not ever expected to change. They are reported in the detatched ASCII header files as independent fields.

5. Output Data

While the EMIT input and output data products delivered to the DAAC use their formatting conventions, the system operates internally on data products stored as binary data cubes with detatched human-readable ASCII header files. The precise formatting convention adheres to the ENVI standard, which can be accessed (Dec. 2019) at https://www.harrisgeospatial.com/docs/ENVIHeaderFiles.html. The header files all consist of data fields in equals-sign-separated pairs, and describe the layout of the file. The L1b stage output is a **radiance** cube, representing radiance at sensor in μW nm^{-1} cm^{-2} sr^{-1} measured by the EMIT instrument. It is geographically projected and stored in Band-Interleaved-by-Line(BIL), with size [rows x channels x columns], in IEEE little endian single-precision floating point. A detatched header file holds information on wavelength calibration, channel response full width at half maximum, and map projection information, following the header convention above. Table 3 Below enumerates all output products.

Output File	Format	Interpretation
Radiance	[rows x bands x columns] float 32, BIL interleave with detached ASCII header	Radiance at sensor in μW nm^{-1} cm^{-2} sr^{-1}

Table 3: Output files

6. Calibration, uncertainty characterization and propagation, and validation

Achieving the EMIT instrument sensitivity rests on a foundation of very accurate instrument calibration. Radiance uncertainty comes from several sources. One is systematic error related to calibration, such as: (1) measurement uncertainties in measurements used for the spectral or radiometric calibration process; (2) modeling error due to algorithm simplifications and approximations, which make them unable to represent the actual spectral and radiometric properties at perfect fidelity; and (3) drift in calibration over time due to degradation. Other uncertainties relate to the measurement noise, which is a random component of each measurement. The measurement noise can be further decomposed into a signal independent portion caused mainly by instrument thermal and electronic state, and a signal dependent portion induced by photon shot noise counting statistics. All uncertainties have some degree of correlation across channels. But for simplicity the EMIT mission characterizes and reports Level 1a radiance uncertainty on a per-channel basis. Systematic uncertainties will be characterized and reported separately through detailed study, but record random measurement noise, written $\sigma_{meas}(\lambda, L)$ directly within the L1a product itself. The model adds known noise sources in quadrature, and accounts for the number of detector readout events added to form each spectrum:

$$\sigma_{meas}(\lambda, L) = \sqrt{\sigma_{shot}(\lambda, L)^2 + \sigma_{dark}(\lambda)^2 + \sigma_{read}^2 + \sigma_{quant}^2} \; / \; \sqrt{n_{read}}$$

Where $\sigma_{shot}(\lambda, L)$ is the standard deviation of photon shot noise, $\sigma_{dark}(\lambda)$ is the dark current contribution, σ_{read} is uncertainty due to readout noise, and σ_{quant} represents truncation-related error due to finite precision storage. We characterize these in advance from laboratory data, and update the model only as needed during the mission. To simplify the data products, we represent the uncertainties above using a simplified functional form, writing the total measurement noise as an independent function of the radiance signal level for each channel. This spectrally-defined function is independent for each acquisition and recorded in the metadata as the three wavelength-indexed functions $\eta_1(\lambda)$, $\eta_2(\lambda)$, and $\eta_3(\lambda)$. The total radiance uncertainty, in noise-equivalent change in radiance units, can then be computed efficiently for any channel as:

$$\sigma_{meas}(\lambda, L) \approx \eta_1(\lambda)\sqrt{\eta_2(\lambda)L(\lambda)} + \eta_3(\lambda) \quad (13)$$

For simplicity, the uncertainty model presumes measurement noise appears as a Gaussian distribution centered on the true radiance. This is not a perfect representation of the error distribution, but enables easy analytical error propagation in subsequent algorithms.

Radiance data is typically validated in flight by acquiring in-situ measurements of surface and atmosphere conditions, and then predicting the resulting measurement using radiative transfer models (RTMs) such as MODTRAN (Berk et al., 2016; 2016b), or the 6S code used in routines like ATREM (Thompson et al., 2019). An example appears in Figure 6 below, which compares two radiative transfer model predictions over a calibration/validation experiment site using remote data from the AVIRIS-NG instrument (Babu et al., 2019). The left panel illustrates the field validation protocol. The field team deploys handheld spectroradiiometers in a grid pattern subtending a wide area of the playa for a uniform spatial average. They return periodically to a reference standard target, the spectralon panel on the tripod at center. This allows a conversion to absolute reflectance values: the radiance from the playa is ratioed against that of the standard panel. We correct this ratio to account for the Bidirectional Reflectance Function of the spectralon target at the given solar zenith, and the intrinsic reflectance signature of the spectralon itself. The result is a reflectance measurement which is combined with in-situ sunphotometer estimates of water vapor and Aerosol Optical Thickness. Optionally, we fit the atmospheric parameters dynamically using iterative retrieval techniques such those in the EMIT Level 2A reflectance estimates (Thompson et al., 2018b). Either way, the result is a prediction for the radiance at sensor which can be compared directly to the measurement and check both absolute and relative calibration.

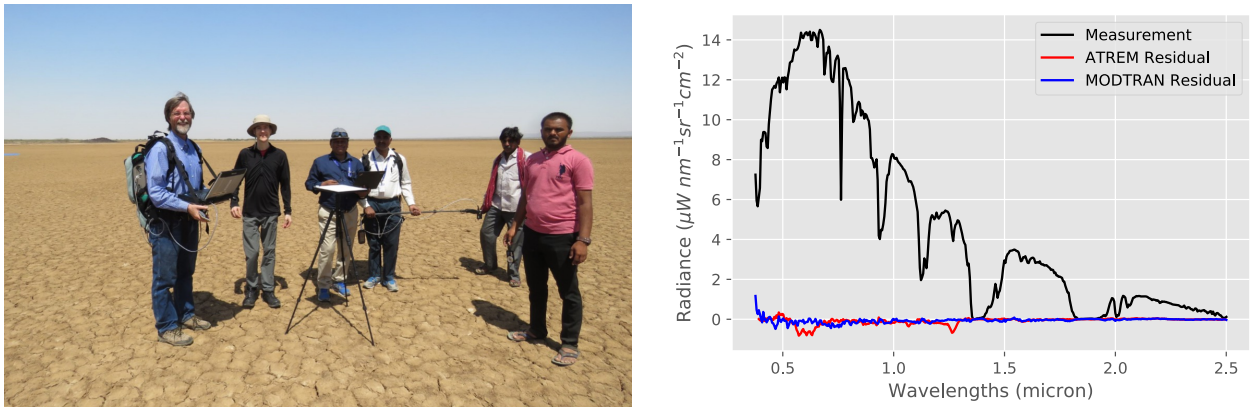

Figure 6: Field validation procedure at Desalpar Playa, India, adapted from Babu et al., (2019). (Left) Field team with in-situ refeerence targets

7. Constraints and Limitations

No constraints or limitations are imposed on the L1B radiometric products. All delivered data will have undergone quality control and should be considered valid calibrations up to the reported uncertainties in input parameters. Unanticipated data corruption due to factors outside the modeling, if discovered, will be reported in peer reviewed literature and/or addenda to this ATBD.

References

Babu, K. N., Mathur, A. K., Thompson, D. R., Green, R. O., Patel, P. N., Prajapati, R. P., ... & Helmlinger, M. C. (2019). An empirical comparison of calibration and validation methodologies for airborne imaging spectroscopy. *CURRENT SCIENCE*, *116*(7), 1101.

Chapman, J., Thompson, D. R., Helmlinger, M. C., Eastwood, M. L., Bue, B. D., Geier, S., Green, R. O., Lundeen, S. R., Olson-Duvall, W. (2019). Spectral and Radiometric Calibration of the Next Generation Airborne Visible Infrared Spectrometer (AVIRIS-NG). *Remote Sensing*, 11(18), 2129.

Berk, A., et al. (2016). Algorithm Theoretic Basis Document (ATBD) for Next Generation MODTRAN®. Spectral Sciences, Inc.: Burlington, MA, USA.

Berk, A., J. van den Bosch, F. Hawes, T. Perkins, P.F. Conforti, G.P. Anderson, R.G. Kennett, P.K. Acharya (2016b). MODTRAN®6.0.0 User's Manual (revision 5). Spectral Sciences, Inc.: Burlington, MA, USA. SSI-TR-685.

Green, R. O., Eastwood, M. L., Sarture, C. M., Chrien, T. G., Aronsson, M., Chippendale, B. J., ... & Olah, M. R. (1998). Imaging spectroscopy and the airborne visible/infrared imaging spectrometer (AVIRIS). *Remote sensing of environment*, *65*(3), 227-248.

Green, R. O., et al. (2011), The Moon Mineralogy Mapper (M^3) imaging spectrometer for lunar science: Instrument description, calibration, on-orbit measurements, science data calibration and on-orbit validation, *J. Geophys. Res.*, 116, E00G19, doi:10.1029/2011JE003797.

Murchie, S. L., Arvidson, R. E., Bedini, P., Beisser, K., Bibring, J. P., Bishop, J., and others and Des Marais, D. (2004). CRISM (compact reconnaissance imaging spectrometer for Mars) on MRO (Mars reconnaissance orbiter). *Instruments, Science, and Methods for Geospace and Planetary Remote Sensing* 5660, 66-77.

Thompson, D. R., Gao, B. C., Green, R. O., Roberts, D. A., Dennison, P. E., & Lundeen, S. R. (2015). Atmospheric correction for global mapping spectroscopy: ATREM advances for the HyspIRI preparatory campaign. *Remote Sensing of Environment*, *167*, 64-77.

Thompson, D. R., Boardman, J. W., Eastwood, M. L., Green, R. O., Haag, J. M., Mouroulis, P., & Van Gorp, B. (2018). Imaging spectrometer stray spectral response: In-flight characterization, correction, and validation. *Remote Sensing of Environment*, *204*, 850-860.

Thompson, D. R., Natraj, V., Green, R. O., Helmlinger, M. C., Gao, B. C., & Eastwood, M. L. (2018b). Optimal estimation for imaging spectrometer atmospheric correction. *Remote sensing of environment*, *216*, 355-373.

Thompson, D. R., Guanter, L., Berk, A., Gao, B. C., Richter, R., Schläpfer, D., & Thome, K. J. (2019). Retrieval of atmospheric parameters and surface reflectance from visible and shortwave infrared imaging spectroscopy data. *Surveys in Geophysics*, *40*(3), 333-360.